

## RESEARCH ARTICLE

## Magnetic Resonance in Medicine

# Deep neural network based CEST and AREX processing: Application in imaging a model of Alzheimer's disease at 3 T

Jianpan Huang<sup>1</sup>  | Joseph H. C. Lai<sup>1</sup> | Kai-Hei Tse<sup>2</sup> | Gerald W. Y. Cheng<sup>2</sup> | Yang Liu<sup>1,3</sup> | Zilin Chen<sup>1</sup> | Xiongqi Han<sup>1</sup>  | Lin Chen<sup>4,5,6</sup>  | Jiadi Xu<sup>4,5</sup>  | Kannie W. Y. Chan<sup>1,3,5,7</sup> 

<sup>1</sup>Department of Biomedical Engineering, City University of Hong Kong, Hong Kong, China

<sup>2</sup>Department of Health Technology and Informatics, The Hong Kong Polytechnic University, Hong Kong, China

<sup>3</sup>Hong Kong Centre for Cerebro-Cardiovascular Health Engineering (COCHE), Hong Kong, China

<sup>4</sup>F.M. Kirby Research Center for Functional Brain Imaging, Kennedy Krieger Research Institute, Baltimore, Maryland, USA

<sup>5</sup>Russell H. Morgan Department of Radiology and Radiological Science, The Johns Hopkins University School of Medicine, Baltimore, Maryland, USA

<sup>6</sup>Department of Electronic Science, Fujian Provincial Key Laboratory of Plasma and Magnetic Resonance, Xiamen University, Xiamen, China

<sup>7</sup>City University of Hong Kong Shenzhen Research Institute, Shenzhen, China

## Correspondence

Kannie W. Y. Chan, Department of Biomedical Engineering, City University of Hong Kong, 83 Tat Chee Ave, Kowloon Tong, Hong Kong.

Email: KannieW.Y.C@cityu.edu.hk

## Funding information

Research Grants Council, Grant/Award Numbers: 11102218, PDFS2122-1S01; City University of Hong Kong, Grant/Award Numbers: 7005210, 9680247, 9667198 and 6000660; National Natural Science Foundation of China, Grant/Award Number: 81871409; Hong Kong Centre for Cerebro-Cardiovascular Health Engineering (COCHE)

**Purpose:** To optimize and apply deep neural network based CEST (deepCEST) and apparent exchange dependent-relaxation (deepAREX) for imaging the mouse brain with Alzheimer's disease (AD) at 3T MRI.

**Methods:** CEST and  $T_1$  data of central and anterior brain slices of 10 AD mice and 10 age-matched wild type (WT) mice were acquired at a 3T animal MRI scanner. The networks of deepCEST/deepAREX were optimized and trained on the WT data. The CEST/AREX contrasts of AD and WT mice predicted by the networks were analyzed and further validated by immunohistochemistry.

**Results:** After optimization and training on CEST data of WT mice, deepCEST/deepAREX could rapidly (~1 s) generate precise CEST and AREX results for unseen CEST data of AD mice, indicating the accuracy and generalization of the networks. Significant lower amide weighted (3.5 ppm) signal related to amyloid  $\beta$ -peptide (A $\beta$ ) plaque depositions, which was validated by immunohistochemistry results, was detected in both central and anterior brain slices of AD mice compared to WT mice. Decreased magnetization transfer (MT) signal was also found in AD mice especially in the anterior slice.

**Conclusion:** DeepCEST/deepAREX could rapidly generate accurate CEST/AREX contrasts in animal study. The well-optimized deepCEST/deepAREX have potential for AD differentiation at 3T MRI.

Jianpan Huang and Joseph H. C. Lai contributed equally to this work.

© 2021 International Society for Magnetic Resonance in Medicine

## KEYWORDS

3T MRI, Alzheimer's disease, amyloid  $\beta$ -peptide plaque, apparent exchange-dependent relaxation, chemical exchange saturation transfer, deep neural network

## 1 | INTRODUCTION

CEST imaging, which noninvasively detects molecules containing exchangeable protons, has developed into a promising technology and drawn much interest in the MRI community.<sup>1,2</sup> Previous studies have demonstrated that CEST MRI is capable of mapping amide protons in peptides or proteins, widely known as amide proton transfer (APT),<sup>3–5</sup> and other metabolites such as glucose,<sup>6,7</sup> creatine,<sup>8–10</sup> and glutamate.<sup>11,12</sup> Relayed nuclear Overhauser effects (rNOE) from mobile proteins and lipids, which contribute to Z-spectrum at 0–5 ppm upfield from the water signal, also have been extensively explored.<sup>13–19</sup> Because of such wide range of capabilities, CEST MRI has been applied to image the molecular changes of various diseases. For example, glucose CEST (glucoCEST) and dynamic glucose enhanced (DGE) MRI has been used to detect the abnormal glucose uptake and use in tumor;<sup>6,7,20</sup> APT has been used to detect the amide proton change in glioma<sup>5,21,22</sup> and pH variation in stroke.<sup>3,23,24</sup> Recent studies showed that CEST MRI has potential for detecting the altered glucose utilization (glucoCEST and DGE MRI) and protein aggregation (APT and rNOE) in Alzheimer's disease (AD).<sup>25–29</sup> Similar to CEST mechanism, semi-solid magnetization transfer (MT) contrast exploits the coupling between the macromolecular protons and the mobile protons to detect macromolecules.<sup>30,31</sup> However, CEST effects are prone to be contaminant by the MT and direct water saturation (DS) effects. Hence, some strategies have been proposed to separate/suppress the MT and DS effects from CEST effects.<sup>13,19,32–35</sup>

Although CEST MRI is a promising molecular imaging technique, it usually requires post-processing with expert knowledge to generate contrasts of interest. Currently, many post-processing methods, including MT ratio asymmetry ( $MTR_{asym}$ ) analysis,<sup>3,36</sup> Lorentzian difference analysis,<sup>18,37</sup> multi-pool Lorentzian fitting,<sup>35,38</sup> and other methods,<sup>9,39</sup> have been proposed for CEST data (Z-spectra) analysis and the outcomes are also diverse. This is one of the factors that limit the widespread application of CEST imaging in the clinical field. To simplify and accelerate the post-processing, deep learning based methods have been introduced in CEST data analysis and promising outcomes have been achieved.<sup>40–43</sup> Deep learning techniques are able to learn representations of data with multiple levels of abstraction using deep neural networks.<sup>44</sup> Zaiss et al<sup>43</sup> trained a deep neural network to predict the 9.4T CEST signals (deepCEST) of human brain using the 3T Z-spectra as inputs.<sup>43</sup> Based on

the similar principle, Glang et al<sup>40</sup> introduced a probabilistic deepCEST with uncertainty quantification to accelerate the analysis of human CEST data at 3T. Chen et al<sup>41</sup> applied an artificial neural network to extract multiple CEST properties (ANNCEST) including metabolite (phosphocreatine) concentration, exchange rate, and  $B_0/B_1$  information at a 3T clinical scanner.<sup>41</sup> These 3 studies all used the 1-D Z-spectra as inputs. In another deep learning-based CEST study, Li et al<sup>42</sup> developed a map-wise deep neural network to achieve acceleration, SNR enhancement and  $B_0$  correction of glutamate CEST (GluCEST) imaging. There were some other studies combining the MR fingerprinting or specific acquisition scheme with deep neural network reconstruction.<sup>45–49</sup> These studies indicated the great potential of using deep learning techniques in CEST MRI.

In this study, we optimized and applied the deep neural network based processing method for analyzing the CEST data of mouse brains with AD at 3T MRI. First, we established the deepCEST with reference to previous studies<sup>40,43</sup> for processing the mouse CEST data. The multi-pool (i.e., DS, amide, rNOE, and MT) CEST parameters were accurately extracted by the well optimized deepCEST with faster speed than conventional multi-pool Lorentzian fitting. Because the CEST signal at 3.5 ppm might be partially contributed by other exchangeable protons,<sup>50</sup> we used 3.5 ppm to represent the amide weighted signal at 3.5 ppm in this paper. Second, we proposed to quantify the apparent exchange-dependent relaxation (AREX) parameters using the other optimized deep neural network (deepAREX). Previous studies have shown that the AREX signal, which includes the longitudinal relaxation time ( $T_1$ ) compensation during processing, could generate CEST contrasts that are proportional to the concentration of the exchanging protons.<sup>14,15,19,51–53</sup> The well trained deepAREX was able to quickly and accurately predict the multiple AREX parameters with Z-spectra and  $T_1$  values as inputs. Finally, we applied the deepCEST/deepAREX to analyze the unseen CEST data of AD mouse brains.

## 2 | METHODS

### 2.1 | Animal preparation

All animal experiments were approved by the Animal Ethics Committee and followed the institutional guidelines of Institutional Laboratory Animal Research Unit of City

University of Hong Kong. Ten AD mice (5XFAD, 11 to 12 months old, from the Jackson Laboratory, ME) and 10 age-matched (wild-type) WT (C57BL/6) mice were used in this study.

## 2.2 | MRI experiments

All MRI experiments were performed on a horizontal bore 3T Bruker BioSpec system (Bruker, Ettlingen, Germany). The coils included an 82 mm quadrature volume resonator as a transmitter and a single surface coil as a receiver (both equipped in the Bruker BioSpec system). All animals were anesthetized using 2% isoflurane in a mixture of oxygen (93%) and air gases and then maintained using 1%–1.5% isoflurane during the MRI scan. Mice were placed on the animal bed with head positioned using a bite bar. The body temperature was maintained with a water-heated pad and the respiratory was prudentially monitored for all mice. Before CEST acquisition, the  $B_0$  field over the mouse brain was well adjusted using field-mapping and second-order shimming. The CEST MRI sequence was a continuous-wave (CW) saturation module followed by the rapid acquisition with refocused echoes (RARE) as a readout module. A power ( $B_1$ ) of 0.6  $\mu$ T and a duration ( $t_{\text{sat}}$ ) of 3 s were used for the saturation module. The saturation frequency offsets were swept from  $-20$  to  $20$  ppm, with a 0.25 ppm increment between  $-8$  and  $8$  ppm, a 1 ppm increment between  $-8/8$  and  $-10/10$  ppm, and a 5 ppm increment between  $-10/10$  to  $-20/20$  ppm. Four  $M_0$  images with saturation frequency offset at 200 ppm were acquired and last 3 of them were averaged for Z-spectrum normalization. The readout parameters were as follows: TR = 5 s, TE = 6 ms, FOV =  $18 \times 18 \text{ mm}^2$ , matrix size =  $96 \times 96$ , slice thickness = 2 mm, RARE factor = 32, centric encoding. Hence, the total scan time for each CEST dataset was 23 minutes 15 seconds. The  $T_1$  maps of the mouse brains were measured using variable-TR RARE (RAREVTR) sequence with TR = 0.1 s, 0.3 s, 0.5 s, 0.8 s, 1.1 s, 1.6 s, 2.4 s, 3.0 s, 4.0 s, and 5.0 s, TE = 10 ms, RARE factor = 4, and other aforementioned imaging parameters. The scan time for each  $T_1$  map was 7 minutes 30 seconds. MRI data of 2 adjacent brain slices from coronal orientation were acquired for each mouse (Supporting Information Figure S1). To investigated the actual A $\beta$  plaques deposition in the mouse brain, the immunohistochemistry experiments<sup>54</sup> (details were given in Supporting Information) were performed on 2 representative mice (1 AD and 1 WT) after MRI scanning.

## 2.3 | Conventional data analysis of CEST and AREX

All MRI data analysis was performed using custom-written code in MATLAB (The MathWorks, Natick, MA).

After CEST data acquisition, the raw Z-spectra were calculated by<sup>2,55</sup>:

$$Z_{\text{raw}}(\Delta\omega) = \frac{M_{\text{sat}}(\Delta\omega)}{M_0}, \quad (1)$$

where  $\Delta\omega$  was the frequency offsets of Z-spectra, whereas  $M_{\text{sat}}(\Delta\omega)$  and  $M_0$  represented the steady-state magnetization with saturation at  $\Delta\omega$  and without saturation, respectively. The Z-spectra were first analyzed with conventional multi-pool Lorentzian fitting. Here, a 4-pool Lorentzian fitting (4PLF) model was applied to fit the Z-spectra<sup>14,40,43</sup> and isolate the 4 peaks of DS, 3.5 ppm, rNOE, and MT pools:

$$Z(\Delta\omega) = 1 - \sum_{i=1}^4 L_i(\Delta\omega). \quad (2)$$

Each peak  $L_i$  could be expressed by a Lorentzian-shaped function:

$$L_i(\Delta\omega) = \frac{A_i}{1 + \left[ \frac{\Delta\omega - (\delta_{\text{DS}} + \Delta\delta_i)}{\Gamma_i/2} \right]^2}, \quad (3)$$

where  $A_i$  represented the peak amplitude,  $\Gamma_i$  represented the full-width-at-half-maximum and  $\delta_{\text{DS}} + \Delta\delta_i$  represented the peak position. Here, the  $\delta_{\text{DS}}$  referred to the water resonance offset and was determined by the fitting from the acquired data, whereas the  $\Delta\delta_i$  were set to 0 ppm, +3.5 ppm,  $-3.5$  ppm, and  $-2.5$  ppm for DS, 3.5 ppm, rNOE, and MT pools, respectively. The initial values and bound conditions for the 4PLF were given in Supporting Information Table S1, which were referred to the previous studies<sup>14,40</sup> that were performed under the same saturation power (0.6  $\mu$ T) and at the same field strength (3T) with our study. According to previous studies,<sup>23</sup> CEST effects can be scaled by the  $T_1$  relaxation time of water, because they are mediated by the water pool. Therefore, all Z-spectra were corrected with  $\delta_{\text{DS}}$  after 4PLF and then, the AREX contrasts were calculated to compensate the  $T_1$ -induced scaling effect using following equation<sup>15</sup>:

$$R_i = R_l \left( \frac{1}{Z_{\text{lab}}} - \frac{1}{Z_{\text{ref}, i}} \right), \quad (4)$$

where  $R_l = 1/T_1$ , whereas  $Z_{\text{lab}}$  and  $Z_{\text{ref}, i}$  represented the Z-spectrum values of label and reference, respectively. The  $Z_{\text{lab}}$  and  $Z_{\text{ref}, i}$  could be calculated as:

$$Z_{\text{lab}} = Z_{\text{raw}}; Z_{\text{ref}, i} = 1 - \sum_{j \neq i} L_j, \{1 \leq j \leq 4\}. \quad (5)$$

After the above-mentioned processes, the  $A_i$  and  $R_i$  were used for generating the multi-pool CEST and AREX

contrast maps, respectively, whereas  $\delta_{DS}$  was used for generating the  $B_0$  inhomogeneity map (in ppm).

## 2.4 | Deep neural networks for CEST and AREX

The networks of deepCEST/deepAREX were fully connected neural networks with optimized hidden layers and neurons, as shown in Figure 1A,B. For deepCEST, the inputs were the full Z-spectrum values and the outputs were 9 CEST parameters generated by 4PLF. As for deepAREX, the full Z-spectrum values together with corresponding  $R_1$  ( $1/T_1$ ) values were taken as inputs and outputs were 4 AREX parameters including  $\Delta B_0$ . The activation function of hidden layers was tansig and the activation function of output layer was mapminmax, which was a linear function matching the interval  $[-1, 1]$  to the range of the output data. Network training was only performed on WT data and then the trained networks were applied on both WT and AD data to test the accuracy and generalization. The training process was so-called backpropagation optimization (scaled conjugate gradient backpropagation).<sup>56</sup> Three strategies were adopted to avoid overfitting during training. First, the WT data was randomly divided into 3 sets: training set (70%), validation set (15%), and test set (15%). The training dataset was used to calculate gradient and update network parameters. The validation dataset was used to monitor the training process. The training was stopped if the mean squared error (*mse*) of the validation dataset did not decrease within 20 iterations. The test dataset was used to access the network generality. Second, early stop of training was triggered when following conditions were met: (1) the epoch number reached  $1 \times 10^4$ ; (2) the *mse* on validation dataset became smaller than  $1 \times 10^{-4}$ ; (3) the minimum performance gradient was smaller than  $1 \times 10^{-5}$ . Third, the performance function was set as *msereg*, which included a regularization to penalize large weights and biases during training:  $msereg = \gamma \times msw + (1-\gamma) \times mse$ , where *msw* represented mean squared weights of the network, *mse* represented the mean squared error of training, and  $\gamma$  was the regularization parameter (set to 0.01 here, details were given in Supporting Information Figure S2). The numbers of hidden layers and neurons were carefully optimized to determine the network architectures of deepCEST/deepAREX (the optimization results were shown in Results section). The results of 4PLF and AREX were taken as targets for the training and as references for the testing. Network training and testing were performed on MATLAB on a computer (Intel Core i7, 16 GB memory) equipped with a graphics processing unit (GPU) GEFORCE RTX 2070 (NVIDIA).

## 2.5 | Statistical analysis

All the statistical results were analyzed using GraphPad Prism 8 (GraphPad Software, San Diego, USA). The group quantitative results were presented in the format of mean  $\pm$  SD. Multiple *t* tests using a 2-stage step-up method of Benjamini, Krieger, and Yekutieli with desired false discovery rate (FDR)  $Q = 1\%$  were performed to assess the difference level. Difference with a *P* value of  $< 0.05$  was regarded as significant.

## 3 | RESULTS

### 3.1 | Network optimization

For both deepCEST and deepAREX, 14 networks with hidden layers varied from 1 to 5 and neurons varied from 10 to 200 were trained for optimization. The dataset including 25,937 Z-spectra of 10 WT mouse brains were used for training. Each network was trained for 5 times and the corresponding validation *mse* and epoch number were averaged for comparison. The training results of different network architectures were shown in Figure 1C,D. When the neuron number increased from 10 to 100, the validation *mse* decreased accordingly, indicating the continuous improvement of network performance. However, the validation *mse* increased if the neuron number further increased to 200. Hence, a neuron number of 100 was used in this study. As for the hidden layers, the validation *mse* decreased when the number of hidden layers (100 neurons in each layer) increased from 1 to 3. However, no further improvement was found, whereas more training epochs were required if the hidden layer number further increased to 4 ([4, 100]) or 5 ([5, 100]). Therefore, a hidden layer number of 3 and a neuron number of 100 in each hidden layer were adopted for both deepCEST and deepAREX (Figure 1E,F), which provided the best network performance with appropriate training epochs among the investigated network architectures.

### 3.2 | DeepCEST and deepAREX results of WT and AD mouse brains

After optimization, the selected deepCEST/deepAREX networks were applied to process the Z-spectra of both WT (seen) and AD (unseen) datasets. The pixel-wise regression results for CEST/AREX parameters of all WT mouse brains revealed good correlations of deepCEST/deepAREX predictions with the 4PLF/AREX results, because the Pearson correlation coefficient *R* values of all parameters were above 0.96 (Figure 2). Notably, the *R*



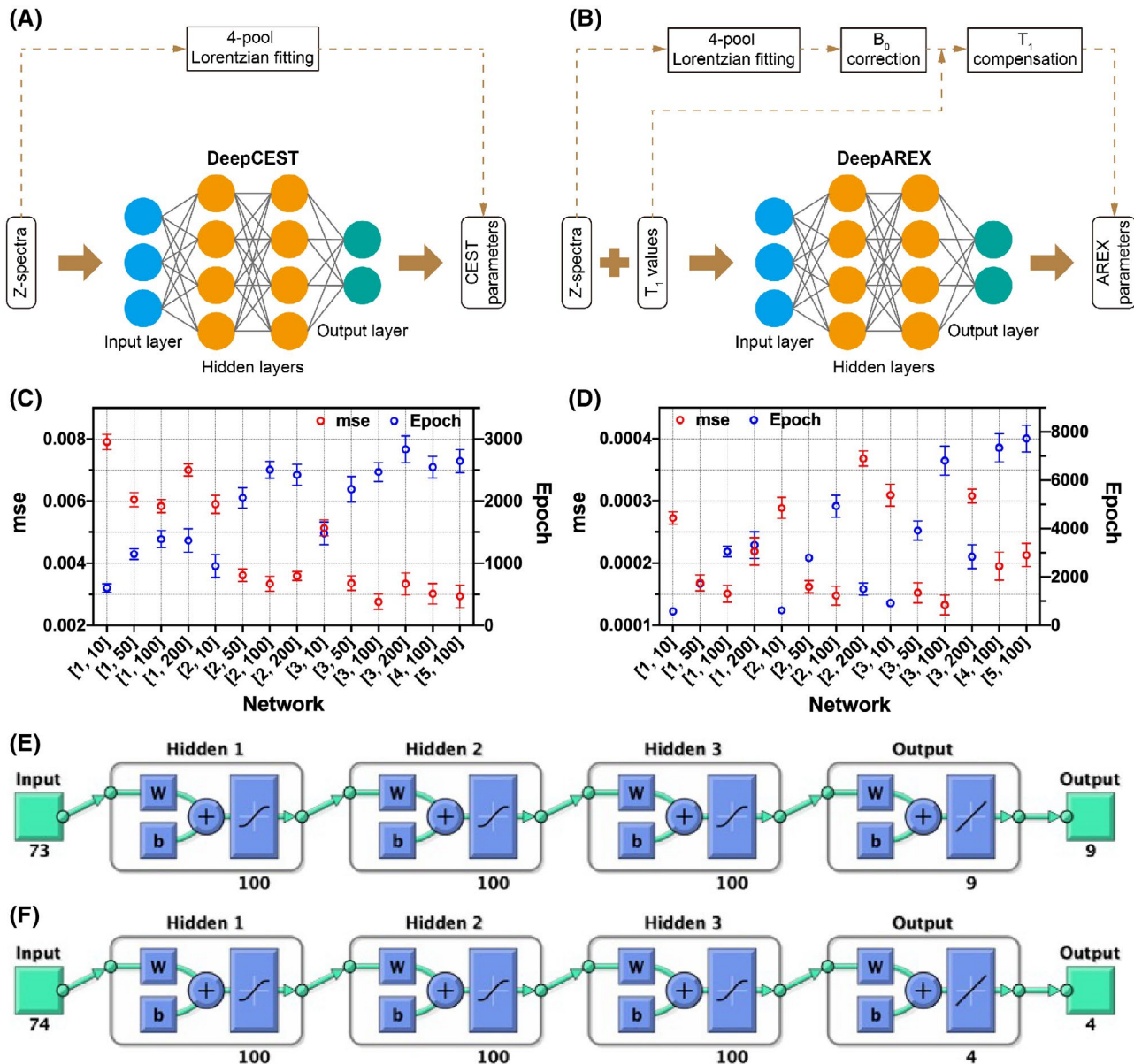


**FIGURE 1** Schematic diagrams and optimization results for deep neural network based CEST (deepCEST) and AREX (deepAREX) processing. Schematic diagrams of (A) deepCEST and (B) deepAREX. Optimization results, including validation mean squared error (*mse*) and epoch number, for different network architectures of (C) deepCEST and (D) deepAREX. Two numbers separated by comma in brackets referred to the number of hidden layers and the number of neurons in each hidden layer, respectively. The optimized network architectures that were used in this study for (E) deepCEST and (F) deepAREX

values of  $\Delta B_0$  for both deepCEST and deepAREX were higher than 0.99, which basically indicated that  $\Delta B_0$  was the most conspicuous feature of a Z-spectrum. Figure 3 showed the representative map results of central and anterior slices of a WT mouse brain generated by 4PLF/AREX and deepCEST/deepAREX. The maps predicted by deepCEST/deepAREX exhibited highly consistent spatial patterns and intensities with difference close to 0 compared to that of 4PLF/AREX. Interestingly, the AREX ( $R_{3.5 \text{ ppm}}$ ,  $R_{\text{rNOE}}$ , and  $R_{\text{MT}}$ ) maps, which have been compensated with  $T_1$  effect, showed more distinguishable brain

structures than the CEST ( $A_{3.5 \text{ ppm}}$ ,  $A_{\text{rNOE}}$ , and  $A_{\text{MT}}$ ) maps (Figure 3). For example, the cerebrospinal fluid (CSF) was clearly discriminated from the parenchyma in all AREX maps, which could be because of the intrinsically different  $T_1$  in these 2 regions (1.6 s for CSF and 1.1 s for parenchyma). Figure 4 showed the representative Z-spectra, together with corresponding CEST results generated by 4PLF and deepCEST, of gray matter (GM), white matter (WM), and CSF. We can see that both methods generated accurate Z-spectra (red solid lines) that matched the raw Z-spectra (black hollow dots) with small residuals (plots

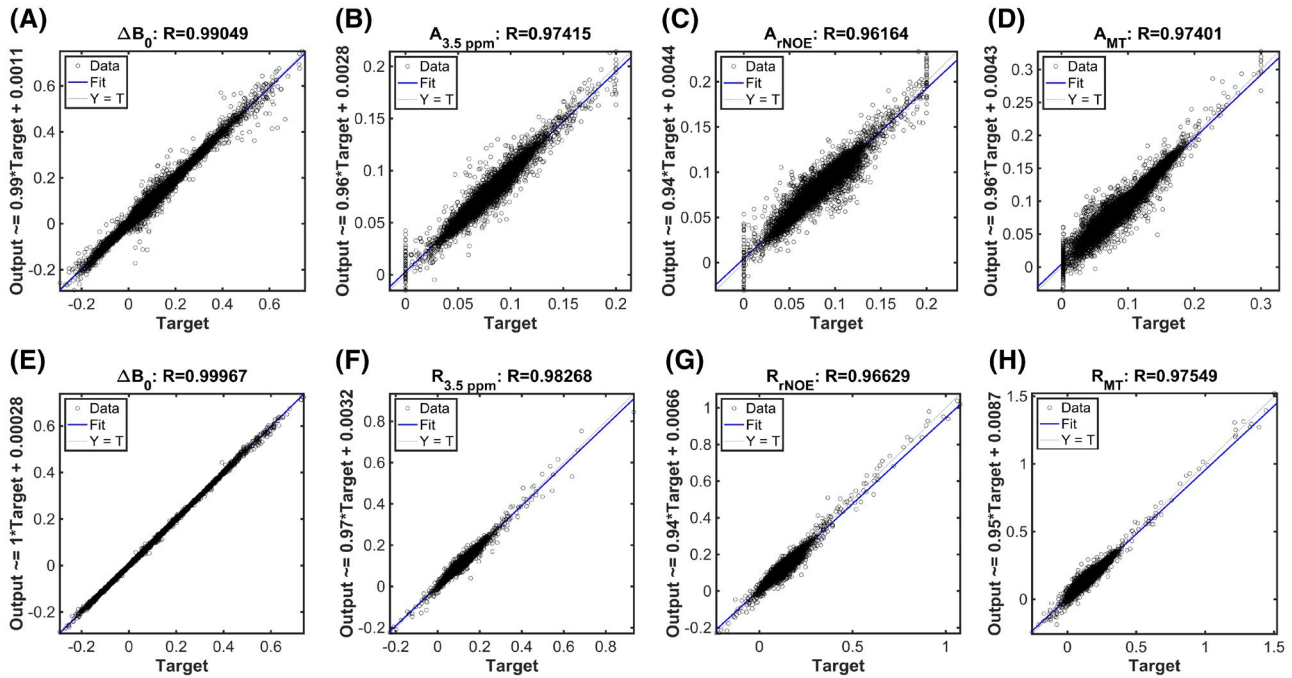


**FIGURE 2** Pixel-wise regression plots of CEST parameters ([A]  $\Delta B_0$  in ppm; [B]  $A_{3.5 \text{ ppm}}$ ; [C]  $A_{\text{rNOE}}$ ; [D]  $A_{\text{MT}}$ ) and AREG parameters ([E]  $\Delta B_0$  in ppm; [F]  $R_{3.5 \text{ ppm}}$ ; [G]  $R_{\text{rNOE}}$ ; [H]  $R_{\text{MT}}$ ) for the training data of all WT mice.  $R_i$  values were presented in  $\text{s}^{-1}$ . Outputs were the results of deepCEST/deepAREX, whereas the targets were the results of 4PLF/AREX

in the last row). The CEST peaks of 4 proton pools were also given at the bottom of coordinate frames. The differences between 4PLF and deepCEST were found to be extremely small ( $<0.004$ ) at the interested offsets ( $\pm 3.5$  and  $-2.5$  ppm). Generally, GM showed larger 3.5 ppm signal than rNOE signal and WM showed larger rNOE signal than 3.5 ppm signal, whereas the CSF showed smallest MT signal among 3 regions.

We, then, applied the optimized deepCEST/deepAREX on the unseen dataset of 10 AD mice to study the generalization of networks and the CEST/AREX signal changes in AD mouse brains. Figure 5 showed the pixel-wise regression results for CEST/AREX parameters of all AD mouse brains. Although most  $R$  values of CEST/AREX parameters (except the  $R$  value in Figure 5A) were slightly lower than that of training dataset (Figure 2), they still stayed at high levels, indicating good correlations of the deepCEST/deepAREX predictions with the 4PLF/AREX results on the unseen AD data as the lowest  $R$  was 0.94 (Figure 5G). This supported that the trained deepCEST/deepAREX had generalization to the CEST data of different types of mice obtained using the same CEST protocol. Comparisons of CEST/AREX maps between AD and WT mouse brains were shown in Figure 6. In general, the rNOE maps ( $A_{\text{rNOE}}$  and  $R_{\text{rNOE}}$ ) of both central and anterior brain slices of AD mouse were comparable to that of WT mouse. However, the 3.5 ppm maps ( $A_{3.5 \text{ ppm}}$  and  $R_{3.5 \text{ ppm}}$ ) of both central and anterior brain slices of AD mouse showed obvious hypointensity compared to that of

WT mouse. Interestingly, the MT maps exhibited inconsistent signal changes in the central and anterior brain slices. Slight hypointensity of MT signal was observed in the central brain slice of AD mouse compared to WT mouse (Figure 6A,C), whereas this hypointensity became more apparent in the anterior brain slice (Figure 6B,D). These observations were further validated by the group comparing results shown in Figure 7. The  $A_{3.5 \text{ ppm}}$  signals of AD mice were significantly lower than that of WT mice in both the central ( $0.068 \pm 0.005$  versus  $0.076 \pm 0.004$ ,  $P < 0.001$ ) and anterior ( $0.070 \pm 0.005$  vs.  $0.077 \pm 0.004$ ,  $P = 0.002$ ) brain slices (Figure 7A,B). These lower signals remained significant after  $T_1$  correction, as the  $R_{3.5 \text{ ppm}}$  results shown in Figure 7C,D (central:  $0.098 \pm 0.009 \text{ s}^{-1}$  vs.  $0.109 \pm 0.005 \text{ s}^{-1}$ ,  $P = 0.002$ ; anterior:  $0.096 \pm 0.009 \text{ s}^{-1}$  vs.  $0.106 \pm 0.004 \text{ s}^{-1}$ ,  $P = 0.003$ ). Similar to the observation in Figure 6, no substantial differences between AD and WT mice were found in  $A_{\text{rNOE}}$  (central:  $0.074 \pm 0.007$  vs.  $0.075 \pm 0.007$ ,  $P = 0.795$ ; anterior:  $0.078 \pm 0.006$  vs.  $0.077 \pm 0.006$ ,  $P = 0.611$ ) and  $R_{\text{rNOE}}$  (central:  $0.107 \pm 0.010 \text{ s}^{-1}$  vs.  $0.108 \pm 0.014 \text{ s}^{-1}$ ,  $P = 0.952$ ; anterior:  $0.112 \pm 0.011 \text{ s}^{-1}$  vs.  $0.107 \pm 0.009 \text{ s}^{-1}$ ,  $P = 0.281$ ). As for MT, lower signal was detected in the central brain slices of AD mice compared to that of WT mice, but not significant ( $A_{\text{MT}}$ :  $0.104 \pm 0.004$  vs.  $0.110 \pm 0.008$ ,  $P = 0.052$ ;  $R_{\text{MT}}$ :  $0.164 \pm 0.005 \text{ s}^{-1}$  vs.  $0.169 \pm 0.013 \text{ s}^{-1}$ ,  $P = 0.330$ ). However, the MT signal of the anterior brain slices of AD mice was obviously lower than that of WT mice ( $A_{\text{MT}}$ :  $0.093 \pm 0.005$  vs.  $0.101 \pm 0.006$ ,  $P = 0.008$ ;  $R_{\text{MT}}$ :  $0.145 \pm 0.006 \text{ s}^{-1}$  vs.  $0.152 \pm$

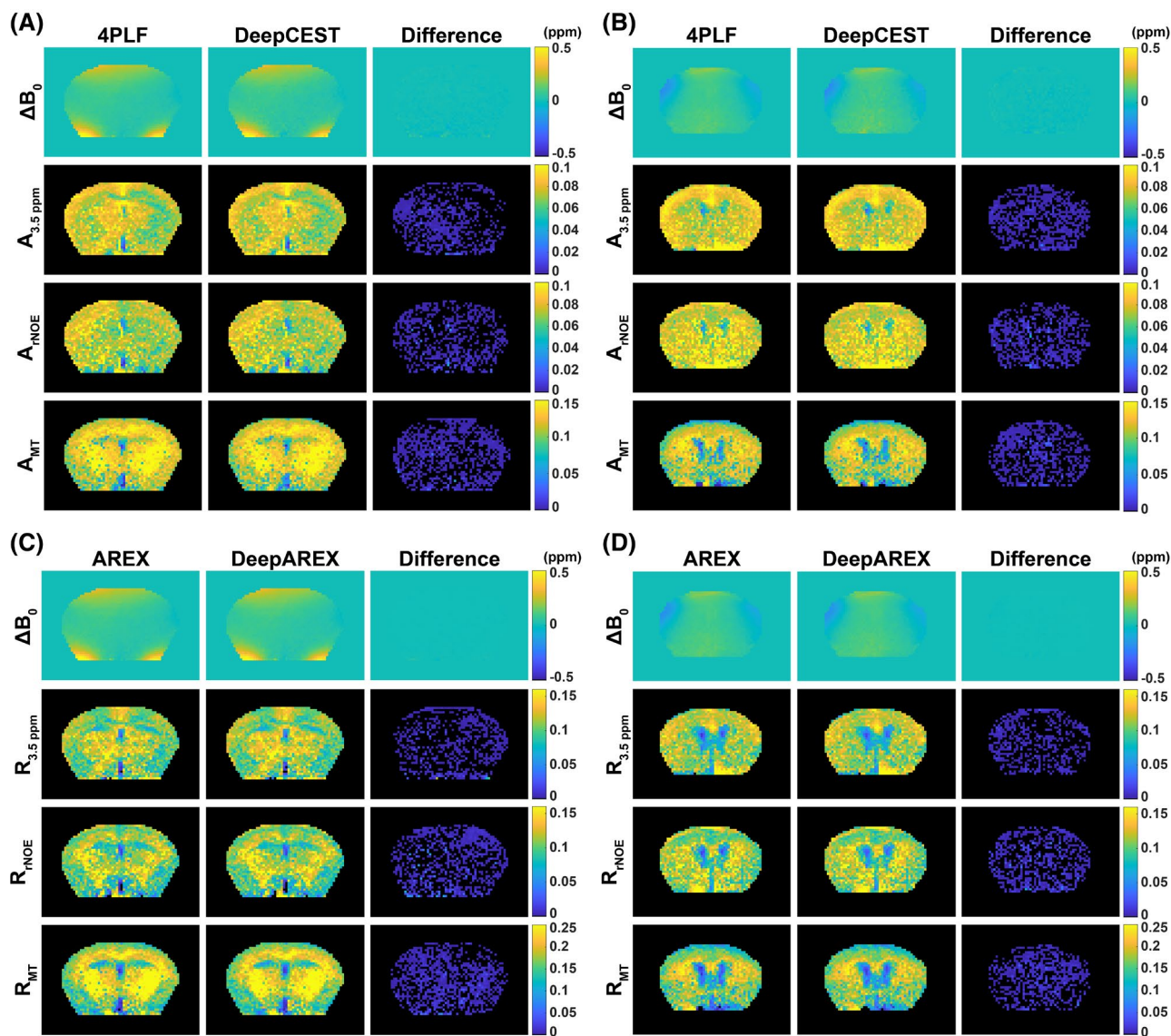


**FIGURE 3** Representative map results of deepCEST/deepAREX, compared to map results of 4PLF/AREX, for WT mouse brain.  $\Delta B_0$  and CEST maps generated by 4PLF and deepCEST, together with their difference, for (A) central and (B) anterior slices.  $\Delta B_0$  and AREX maps generated by AREX and deepAREX, together with their difference, for (C) central and (D) anterior slices.  $R_i$  values were presented in  $\text{s}^{-1}$

$0.009 \text{ s}^{-1}$ ,  $P = 0.039$ ). Figures 6 and 7 were generated using deepCEST/deepAREX, corresponding results generated by conventional 4PLF/AREX were shown in Supporting Information Figures S3 and S4. In general, the differences between AD and WT mice detected by 2 methods were almost the same, except a slight improvement in significance level of anterior  $R_{\text{MT}}$  difference (Figure 7D and Supporting Information Figure S4D). The regression results of CEST/AREX parameters generated by 2 methods for all mice were also shown in Figure S5, which revealed superb correlations ( $R$  values  $>0.998$ ) of deepCEST/deepAREX predictions with 4PLF/AREX results on the subject based comparisons. We also compared the  $T_1$  values of 2 types of mice, interestingly,  $T_1$  values of AD mice were significantly lower than that of WT mice in both central slice ( $1087 \pm 37 \text{ ms}$  vs.

$1128 \pm 27 \text{ ms}$ ,  $P = 0.012$ ) and anterior slice ( $1109 \pm 36 \text{ ms}$  vs.  $1156 \pm 30 \text{ ms}$ ,  $P = 0.005$ ), as shown in Figure 8. Similar observation was reported in a previous study where the same 5XFAD mice at similar age were used.<sup>57</sup> This well explained why the differences (3.5 ppm and MT) between WT and AD became less significant in AREX than in CEST, because the  $T_1$  contribution was excluded. Therefore, AREX results were important to reveal chemical exchange-related changes induced by protein aggregation in AD.

### 3.3 | Immunohistochemistry validation

Immunohistochemistry experiments were performed to assess the actual  $A\beta$  plaques in mouse brain and results



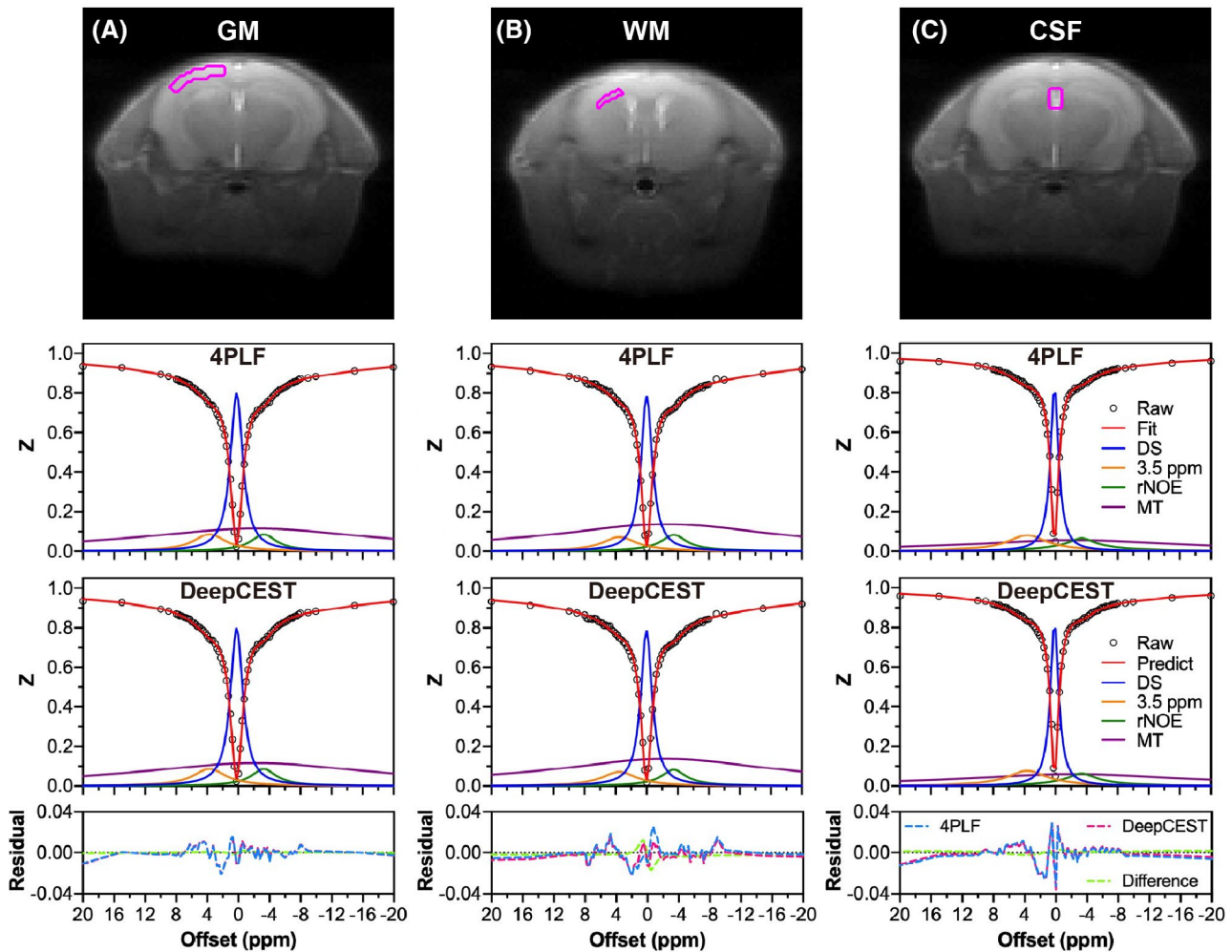


**FIGURE 4** Representative 4PLF and deepCEST processing results of Z-spectra in (A) gray matter (GM), (B) white matter (WM) and (C) cerebrospinal fluid (CSF). Magenta frames in  $M_0$  images indicated the region of interest (ROI) selections in 3 brain regions for calculating the representative Z-spectra. Here, ROIs of GM, WM, and CSF were placed on cortex, corpus callosum, and central CSF, respectively. Residuals were calculated by subtracting 2 Z-spectra: Residual (4PLF) = Z-spectra (Raw) – Z-spectra (Fit); Residual (DeepCEST) = Z-spectra (Raw) – Z-spectra (Predict); Residual (Difference) = Z-spectra (Fit) – Z-spectra (Predict)

were shown in Figure 9. No  $A\beta$  plaque was found in both central and anterior brain slices of WT mouse (Figure 9A,C). On the contrary, numerous  $A\beta$  plaques were clearly observed in both central and anterior brain slices of AD mouse at studied age (Figure 9B,D). These results were similar with previous studies showing that substantial  $A\beta$  plaques appeared in brain of 5xFAD mice at 10 months of age.<sup>58</sup> Because of the large differences in thickness and resolution, it was inaccurate to do a pixel-by-pixel correlation between CEST and histology images. Instead, we calculated the ratio of pixels occupied by plaques (plaque pixels/whole brain pixels) to estimate the severity of protein aggregation in these 2 slices. The ratios of pixel occupied by plaques were found to be 11.8% and 5.1% in central and anterior slices of AD mouse, respectively. These resembled the CEST findings (Figure 7). For example, the percentages of decreased 3.5 ppm signal of

AD mice compared to WT mice were found to be 10.5% and 10.1% for  $A_{3.5 \text{ ppm}}$  and  $R_{3.5 \text{ ppm}}$ , respectively, in the central slice, whereas they became slightly lower in the anterior slice with values of 9.1% and 9.4% for  $A_{3.5 \text{ ppm}}$  and  $R_{3.5 \text{ ppm}}$ , respectively.

## 4 | DISCUSSION

We optimized and applied the deepCEST/deepAREX to analyze the CEST data of mouse brains at 3T and results showed that deepCEST/deepAREX generated accurate CEST/AREX contrasts at a much faster speed compared to conventional 4PLF/AREX methods. Importantly, substantial differences in CEST/AREX contrasts between WT and AD mice were detected by deepCEST/deepAREX. Deep neural network based CEST for human studies



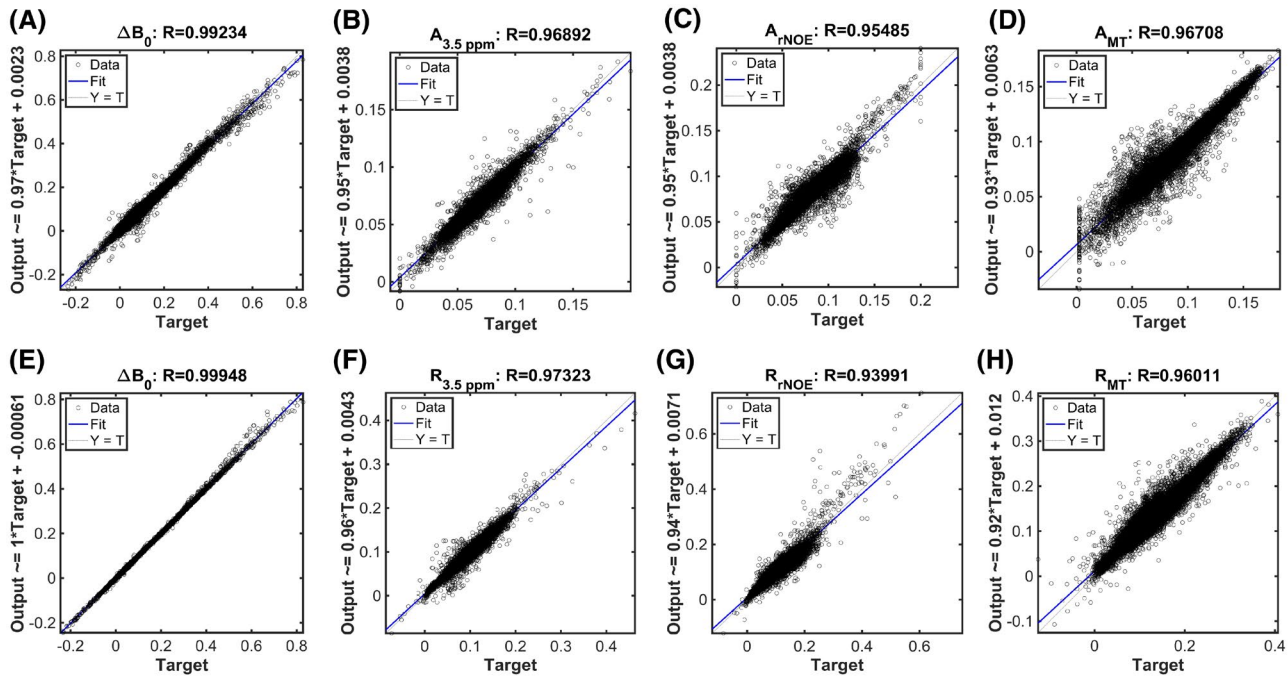


**FIGURE 5** Pixel-wise regression plots of CEST parameters ([A]  $\Delta B_0$  in ppm; [B]  $A_{3.5 \text{ ppm}}$ ; [C]  $A_{rNOE}$ ; [D]  $A_{rMT}$ ) and AREX parameters ([E]  $\Delta B_0$  in ppm; [F]  $R_{3.5 \text{ ppm}}$ ; [G]  $R_{rNOE}$ ; [H]  $R_{rMT}$ ) for the testing data of all AD mice.  $R_i$  values were presented in  $s^{-1}$ . Outputs were the results of deepCEST/deepAREX, whereas the targets were the results of 4PLF/AREX

have already shown high feasibility and promising outcomes.<sup>40,41,43</sup> In this study, we applied deepCEST/deepAREX on CEST data of mice. The mouse brain is much smaller than the human brain, resulting in smaller data size that could be used for training (25,937 Z-spectra from 10 mice here compared to 135,752 Z-spectra from 3 human subjects in previous study<sup>40</sup>). Nevertheless, our results demonstrated that the deep neural network based CEST was also applicable on mouse study. After well training, the deepCEST with a hidden layer number of 3 and a neuron number of 100 could rapidly predict multiple CEST contrasts with high accuracy ( $R > 0.96$  for training data in Figure 2A-D and  $R > 0.95$  for testing data in Figure 5A-D). Conventional 4PLF took  $\sim 20$  s to generate multiple CEST contrast maps for a single mouse brain slice, whereas deepCEST only took  $\sim 1$  s to predict the comparable results on the same computer. This time difference could be enlarged when applying deepCEST on the human brain, as reported in previous study (i.e.,  $\sim 1$  s for deepCEST and  $\sim 10$  minutes for 4PLF).<sup>40</sup> Notably, we for the first time demonstrated that deep neural networks were capable of predicting the AREX parameters. Compared to CEST, AREX with  $T_1$  compensation could provide purely chemical exchange-related contrasts.<sup>15,51–53,59</sup> Although 2 additional procedures were involved in AREX calculation (i.e.,  $B_0$  correction and  $T_1$  compensation) (Figure 1B) the trained deepAREX could also quickly generate multiple AREX contrasts with high accuracy ( $R > 0.96$  for training

data in Figure 2E-H  $R > 0.93$  for testing data in Figure 5E-H) and similar speed to deepCEST ( $\sim 1$  s). DeepAREX could be useful especially for imaging subjects containing multiple components with substantially different  $T_1$  values. For example, CSF region became more distinguishable from parenchyma region in AREX maps compared to CEST maps (Figures 3 and 6), due the substantially different  $T_1$  values in these 2 regions (Figure 8).

Although the deepCEST/deepAREX were only trained on CEST data of WT mice, they predicted accurate results on unseen CEST data of AD mice as well (Figure 5). This indicated that the networks were not overfitting and had generalization to CEST data of mouse brain. We found that the significant lower 3.5 ppm signals in the central ( $A_{3.5 \text{ ppm}}: P < 0.001$ ;  $R_{3.5 \text{ ppm}}: P = 0.002$ ) and anterior ( $A_{3.5 \text{ ppm}}: P = 0.002$ ;  $R_{3.5 \text{ ppm}}: P = 0.003$ ) brain slices of AD mice compared to WT mice (Figure 7). Similar finding was also reported by previous study on animal AD models.<sup>27,29</sup> However, some other studies observed an increase in APT weighted (APTw) signal in human AD and mild cognitive impairment (MCI).<sup>60,61</sup> We speculate there are 2 reasons for these contradicting findings: one is the analysis methods. APTw signal calculated by  $MTR_{asym}$  is a mixed contrast, which includes multiple effects such as APT,  $rNOE$ , and MT. Another one is the limitation of AD mouse models, which only represent part of AD neuropathology in humans. 5XFAD mouse model used in this study is characterized by extracellular A $\beta$  plaques,

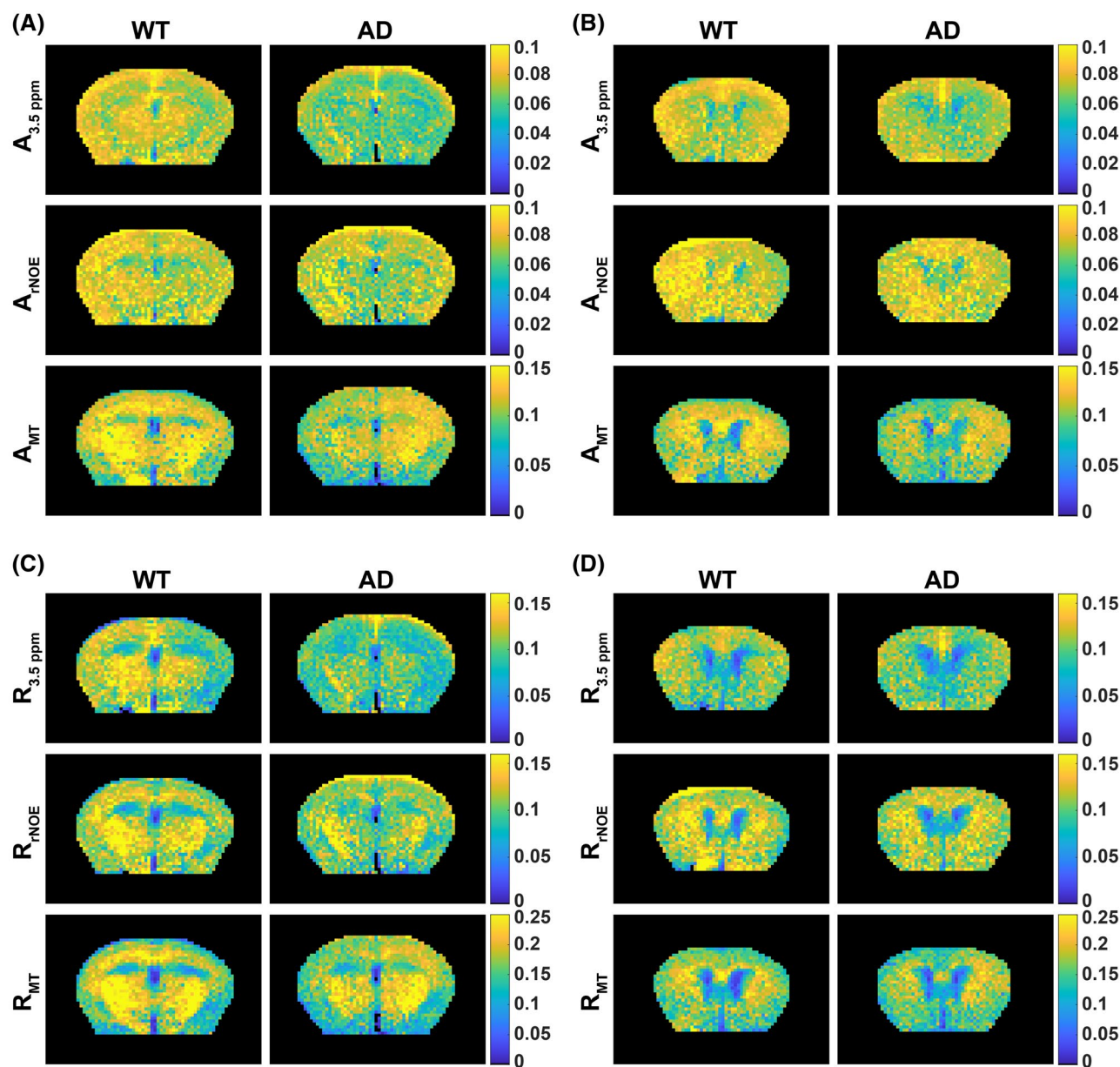


**FIGURE 6** Representative CEST/AREX maps of WT and AD brains that were generated by deepCEST/deepAREX. CEST maps ( $A_{3.5 \text{ ppm}}$ ,  $A_{r\text{NOE}}$ , and  $A_{\text{MT}}$ ) of (A) central and (B) anterior slices. AREX maps ( $R_{3.5 \text{ ppm}}$ ,  $R_{r\text{NOE}}$ , and  $R_{\text{MT}}$ ) of (C) central and (D) anterior slices.  $R_i$  values were presented in  $\text{s}^{-1}$

whereas neuropathologies in human AD at the late stage include the accumulation of both extracellular  $A\beta$  plaques and intracellular neurofibrillary tangles (NFTs). NFTs consist of hyperphosphorylated and misfolded tau protein.<sup>62</sup> Nevertheless, the decreased 3.5 ppm signals could be related to the deposition of  $A\beta$  plaques in AD mouse brain, which was validated by the immunohistochemistry results (Figure 9). Both the central and anterior brain slices of AD mouse with 6E10 staining showed massive  $A\beta$  plaques in most of the brain regions, which resembled the previous results performed on 5XFAD mice at similar age,<sup>58</sup> whereas no  $A\beta$  plaque was found in age-matched

WT mouse brain. Moreover, ratios of pixel occupied by plaques were found to be similar with the percentages of decreased 3.5 ppm signal in AD mice (Figures 7 and 9), indicating that the decreased 3.5 ppm signal in AD mice was largely attributed to the  $A\beta$  plaque deposition in brain. A recent study at high field has reported that pH change could lead to observable changes in creatine CEST (CrCEST) contrast in tauopathy (Tau) and  $A\beta$  amyloidosis (APP) AD mouse models.<sup>63</sup> They found significantly decreased creatine CEST contrast in AD mice, at the same time the concentration of creatine remained unchanged from the  $^{31}\text{P}$  and proton MRS results. This indicated that

**FIGURE 7** Group comparison of CEST/AREX results between WT ( $n = 10$ ) and AD ( $n = 10$ ) mice that were generated by deepCEST/deepAREX. Comparison of CEST parameters ( $A_{3.5\text{ ppm}}$ ,  $A_{\text{rNOE}}$ , and  $A_{\text{MT}}$ ) between WT and AD for (A) central and (B) anterior slices. Comparison of AREX parameters ( $R_{3.5\text{ ppm}}$ ,  $R_{\text{rNOE}}$ , and  $R_{\text{MT}}$ ) between WT and AD for (C) central and (D) anterior slices.  $R_i$  values were presented in  $\text{s}^{-1}$ . Significance levels:  $*P < 0.05$ ,  $**P < 0.01$ , and  $***P < 0.001$

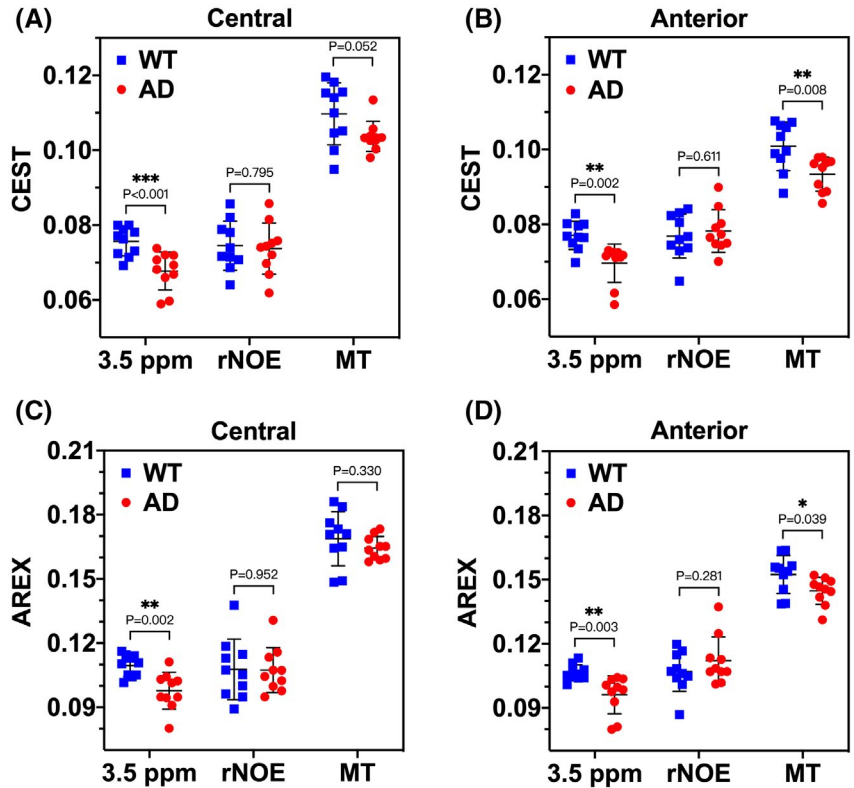


**FIGURE 8** Comparison of  $T_1$  results between WT and AD mice. (A) Representative  $T_1$  maps of WT and AD mouse brains, including both central and anterior slices. (B) Group comparison of  $T_1$  values between WT ( $n = 10$ ) and AD ( $n = 10$ ) mouse brains in both central and anterior slices

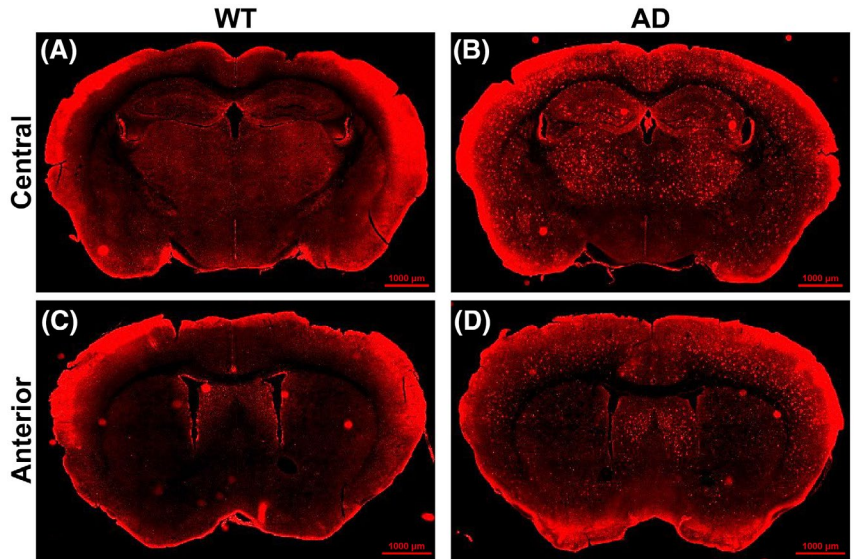
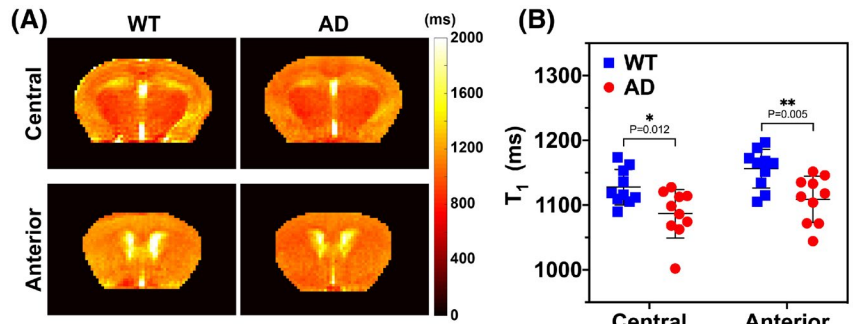


**FIGURE 9** Immunohistochemistry (6E10 staining) results of (A,C) WT and (B,D) AD mouse brains, including both (A,B) central and (C,D) anterior slices



the decrease in CrCEST contrast might be attributed to the decrease in the Cr exchange rate induced by the reduced intracellular cerebral pH, which could be a consequence of neuroinflammation involved in the development of AD.<sup>64,65</sup> Further studies will be helpful to examine whether the pH changes in AD brains would lead to observable changes in amide contrast. The rNOE signals including  $A_{\text{rNOE}}$  and  $R_{\text{rNOE}}$  in both central and anterior brain slices of AD mice were comparable to that of WT mice. The MT signals exhibited difference between AD and WT mice, but with less sensitivity than 3.5 ppm signals. Slightly lower MT signal ( $A_{\text{MT}}$ :  $P = 0.052$ ;  $R_{\text{MT}}$ :  $P = 0.330$ ) was detected in the central brain slice of AD mice compared

to WT mice, whereas significant lower MT signal ( $A_{\text{MT}}$ :  $P = 0.008$ ;  $R_{\text{MT}}$ :  $P = 0.039$ ) was detected in the anterior brain slice of AD mice. The MT signal change could have various and complicated contributions because it came from multiple types of macromolecules. Some studies have reported a decreased MT signal in the AD brain, which might be attributed by surface-hydrophobicity of  $A\beta$  plaque deposition, demyelination, axon loss, and structure damage.<sup>66–72</sup> On the other hand, some studies also reported an increased MT signal in early APP/PS1 transgenic mouse model, which was ascribed to the  $A\beta$  plaque itself.<sup>73,74</sup> We speculated that these factors together resulted in a variously lower MT signal in 5XFAD

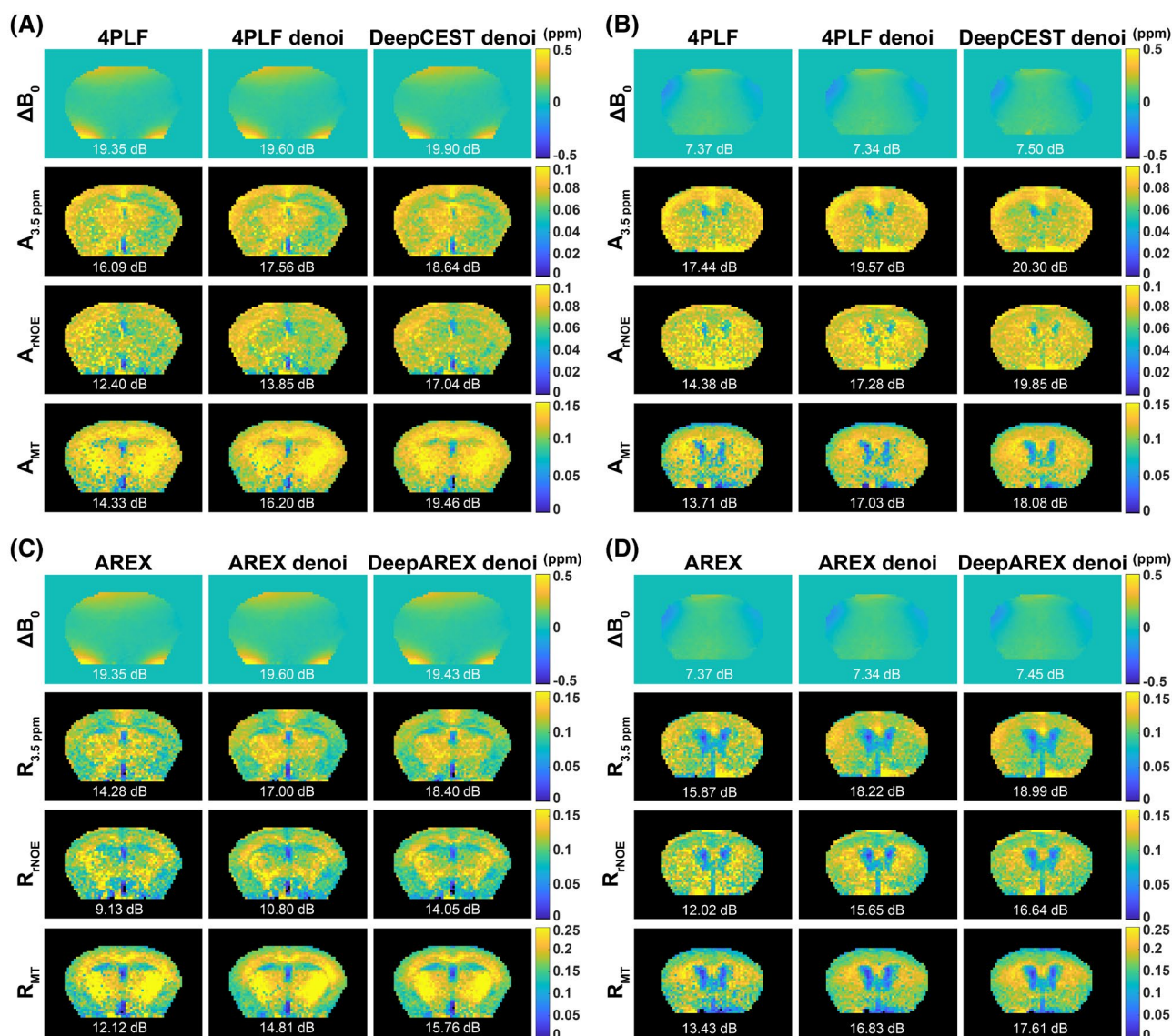


**FIGURE 10** Map results of deepCEST/deepAREX with denoising, compared to map results of 4PLF/AREX without/with denoising, for WT mouse brain.  $\Delta B_0$  and CEST maps generated by 4PLF without denoising, 4PLF with denoising and deepCEST with denoising, for (A) central and (B) anterior slices.  $\Delta B_0$  and AREX maps generated by AREX without denoising, AREX with denoising and deepAREX with denoising, for (C) central and (D) anterior slices.  $R_i$  values were presented in  $s^{-1}$ . Numbers inside maps indicated the corresponding SNR values. SNR values were calculated by:  $\text{SNR} = 20 \times \lg(\text{mean}/\text{SD})$

mouse brains (i.e., significant in the anterior slice, but not in the central slice) compared to WT mouse brains, because 5XFAD mouse model exhibited more robust neuron death compared to APP/PS1 mouse model.<sup>75</sup> Further validation on this transgenic mouse model for this MT observation is needed in a future study.

To further explore the performance of deepCEST/deepAREX, their denoising ability was also investigated (details were given in Supporting Information Figures S6-S9). Results showed that both 4PLF/AREX with denoising and deepCEST/deepAREX with denoising could effectively generate denoised CEST/AREX contrasts with higher SNR (except the  $\Delta B_0$  maps which were originally smooth) than that of 4PLF/AREX without denoising (Figure 10). Notably, deepCEST/deepAREX with denoising showed slightly higher SNR than 4PLF/AREX with denoising, indicating the intrinsic learning and improving abilities of deep neural networks. Furthermore, deepCEST/deepAREX with denoising showed robustness to resist the added Gaussian noise with the SD of 0.01 and still performed better than 4PLF/AREX with denoising (blue regions of interest [ROIs] in Supporting Information Figure S10C,D). However, when the SD of noise increased to 0.05, both methods failed to produce the correct results (red ROIs in Supporting Information Figure S10C,D). To improve the performance of deepCEST/deepAREX under such high noise interference (although uncommon in CEST studies), data augmentation is one of the effective ways.<sup>40</sup> Moreover, the consistency checking for deepCEST was also performed (Supporting Information Figure S11A). When the Z-spectra reconstructed using the CEST parameters generated by deepCEST were fed back into the corresponding networks, almost the same Z-spectra (differences  $<0.003$ ) and CEST parameters (R values  $>0.99$ ) were generated again (Supporting Information Figure S11B-E).

Although the deepCEST/deep AREX showed promising results, there were still some limitations in the current study. First, none of current CEST post-processing methods is able to generate perfect results that can be regarded as real ground truth. In this study, a low  $B_1$  of 0.6  $\mu\text{T}$  was used for CEST acquisition; therefore, 4PLF worked well and could be regarded as a good reference for deepCEST/deepAREX. Second, the CEST signal at 3.5 ppm was not pure amide signal. This signal might contain partial contributions from other metabolites in the brain,<sup>50</sup> but it could be regarded as amide weighted signal.<sup>76</sup> Third, there was slight  $B_1$  inhomogeneity effect observed at the rim of MT maps (Figure 3 and Supporting Information Figure S12). Because a low  $B_1$  power (0.6  $\mu\text{T}$ ) was used here and the average  $B_1$  relative values over the mouse brain were very close to 1 (Supporting Information Figure S12,  $0.98 \pm 0.08$  in the central slice and  $0.98 \pm 0.06$  in the anterior

slice), the influence of  $B_1$  effect was negligible in the group comparisons where the mean values of the whole brain slices were used. Despite these limitations, our results demonstrated that the currently established deepCEST/deepAREX showed sufficient accuracy, generalization, denoising ability, and consistency on mouse data. When deepCEST/AREX are translated to clinical applications, issues in 2 aspects should be well considered. One aspect is the CEST sequence: (1) CW saturation module should be replaced by a pulsed saturation module because of the specific absorption rate (SAR) issue. (2) The interval of frequency offsets can be appropriately adjusted to reduce scan time, because a scan time of  $>20$  minutes is not ideal in clinical applications. The other aspect is the network training: (1)  $B_1$  correction<sup>59</sup> can be added to deepCEST/deepAREX if the scanner setup has a large  $B_1$  inhomogeneity. (2) Data augmentation involving large  $\Delta B_0$  and noise can be applied to simulate the complicated human brain (larger volume and more structured tissues than the mouse brain), therefore, enhancing the robustness of networks. In this case, the uncertainty quantification proposed in previous study<sup>40</sup> could be added to the networks to guide the data augmentation and give hints about possible error sources during acquisition.

## 5 | CONCLUSION

In this study, we applied the deepCEST to analyze the CEST data of mouse brains at 3T and proposed to use deepAREX to predict the AREX contrasts with  $T_1$  correction. Our results showed that both deepCEST and deepAREX could rapidly generate accurate results with higher speed compared to conventional least squares fitting methods. The generalizations of deepCEST/deepAREX were well validated on the unseen data of AD mice. Interestingly, significantly lower amide weighted (3.5 ppm) signal related to A $\beta$  plaque depositions, which were validated by immunohistochemistry results, were detected in AD mice compared to age-matched WT mice. Decreased MT signal was also found in AD mice and it was significant in anterior slice. These results indicated that well-established deepCEST/deepAREX have great potential for AD differentiation at a clinical-field-strength 3T MRI.

## ACKNOWLEDGMENTS

This work was supported by the Research Grants Council (11102218, PDFS2122-1S01), City University of Hong Kong (7005210, 9680247, 9667198 and 6000660), National Natural Science Foundation of China (81871409), and Hong Kong Centre for Cerebro-Cardiovascular Health Engineering (COCHE).

## DATA AVAILABILITY STATEMENT

The code and exemplary data that support the findings of this study are openly available at <https://github.com/JianpanHuang/DeepCESTandDeepAREX>.

## ORCID

Jianpan Huang  <https://orcid.org/0000-0002-4453-8764>

Xiongqi Han  <https://orcid.org/0000-0003-3557-0268>

Lin Chen  <https://orcid.org/0000-0003-0108-4309>

Jiadi Xu  <https://orcid.org/0000-0001-9698-5622>

Kannie W. Y. Chan  <https://orcid.org/0000-0002-7315-1550>

## REFERENCES

- Ward K, Aletras A, Balaban RS. A new class of contrast agents for MRI based on proton chemical exchange dependent saturation transfer (CEST). *J Magn Reson*. 2000;143:79-87.
- Van Zijl PC, Yadav NN. Chemical exchange saturation transfer (CEST): what is in a name and what isn't? *Magn Reson Med*. 2011;65:927-948.
- Zhou J, Payen J-F, Wilson DA, Traystman RJ, van Zijl PC. Using the amide proton signals of intracellular proteins and peptides to detect pH effects in MRI. *Nat Med*. 2003;9:1085-1090.
- Jones CK, Schlosser MJ, Van Zijl PC, Pomper MG, Golay X, Zhou J. Amide proton transfer imaging of human brain tumors at 3T. *Magn Reson Med*. 2006;56:585-592.
- Zhou J, Lal B, Wilson DA, Laterra J, van Zijl PC. Amide proton transfer (APT) contrast for imaging of brain tumors. *Magn Reson Med*. 2003;50:1120-1126.
- Walker-Samuel S, Ramasawmy R, Torrealdea F, et al. In vivo imaging of glucose uptake and metabolism in tumors. *Nat Med*. 2013;19:1067-1072.
- Chan KW, McMahon MT, Kato Y, et al. Natural D-glucose as a biodegradable MRI contrast agent for detecting cancer. *Magn Reson Med*. 2012;68:1764-1773.
- Haris M, Nanga RPR, Singh A, et al. Exchange rates of creatine kinase metabolites: feasibility of imaging creatine by chemical exchange saturation transfer MRI. *NMR Biomed*. 2012;25:1305-1309.
- Chen L, Barker PB, Weiss RG, van Zijl PC, Xu J. Creatine and phosphocreatine mapping of mouse skeletal muscle by a polynomial and Lorentzian line-shape fitting CEST method. *Magn Reson Med*. 2019;81:69-78.
- Cai K, Singh A, Poptani H, et al. CEST signal at 2 ppm (CEST@2 ppm) from Z-spectral fitting correlates with creatine distribution in brain tumor. *NMR Biomed*. 2015;28:1-8.
- Kogan F, Singh A, Debrosse C, et al. Imaging of glutamate in the spinal cord using GluCEST. *Neuroimage*. 2013;77:262-267.
- Cai K, Haris M, Singh A, et al. Magnetic resonance imaging of glutamate. *Nat Med*. 2012;18:302-306.
- Xu X, Yadav NN, Zeng H, et al. Magnetization transfer contrast-suppressed imaging of amide proton transfer and relayed nuclear overhauser enhancement chemical exchange saturation transfer effects in the human brain at 7T. *Magn Reson Med*. 2016;75:88-96.
- Goerke S, Soehngen Y, Deshmane A, et al. Relaxation-compensated APT and rNOE CEST-MRI of human brain tumors at 3 T. *Magn Reson Med*. 2019;82:622-632.
- Zaiss M, Windschuh J, Paech D, et al. Relaxation-compensated CEST-MRI of the human brain at 7 T: unbiased insight into NOE and amide signal changes in human glioblastoma. *Neuroimage*. 2015;112:180-188.
- Zu Z, Xu J, Li H, et al. Imaging amide proton transfer and nuclear overhauser enhancement using chemical exchange rotation transfer (CERT). *Magn Reson Med*. 2014;72:471-476.
- Xu J, Yadav NN, Bar-Shir A, et al. Variable delay multi-pulse train for fast chemical exchange saturation transfer and relayed-nuclear overhauser enhancement MRI. *Magn Reson Med*. 2014;71:1798-1812.
- Jones CK, Huang A, Xu J, et al. Nuclear Overhauser enhancement (NOE) imaging in the human brain at 7 T. *Neuroimage*. 2013;77:114-124.
- Huang J, Han X, Chen L, Xu X, Xu J, Chan KW. Relayed nuclear Overhauser enhancement imaging with magnetization transfer contrast suppression at 3 T. *Magn Reson Med*. 2021;85:254-267.
- Xu X, Chan Kwy, Knutsson L, et al. Dynamic glucose enhanced (DGE) MRI for combined imaging of blood-brain barrier breakdown and increased blood volume in brain cancer. *Magn Reson Med*. 2015;74:1556-1563.
- Paech D, Windschuh J, Oberhollenzer J, et al. Assessing the predictability of IDH mutation and MGMT methylation status in glioma patients using relaxation-compensated multipool CEST MRI at 7.0 T. *Neuro Oncol*. 2018;20:1661-1671.
- Jiang S, Zou T, Eberhart CG, et al. Predicting IDH mutation status in grade II gliomas using amide proton transfer-weighted (APT<sub>w</sub>) MRI. *Magn Reson Med*. 2017;78:1100-1109.
- Zaiss M, Xu J, Goerke S, et al. Inverse Z-spectrum analysis for spillover-, MT-, and T1-corrected steady-state pulsed CEST-MRI-application to pH-weighted MRI of acute stroke. *NMR Biomed*. 2014;27:240-252.
- Tietze A, Blicher J, Mikkelsen IK, et al. Assessment of ischemic penumbra in patients with hyperacute stroke using amide proton transfer (APT) chemical exchange saturation transfer (CEST) MRI. *NMR Biomed*. 2014;27:163-174.
- Huang J, van Zijl PC, Han X, et al. Altered D-glucose in brain parenchyma and cerebrospinal fluid of early Alzheimer's disease detected by dynamic glucose-enhanced MRI. *Sci Adv*. 2020;6:eaba3884.
- Huang J, Xu J, Dong CM, et al. Impaired glucose uptake in mouse brain with Alzheimer's disease detected by dynamic glucose enhanced (DGE) MRI at 3T. *Alzheimers Dement*. 2019;15:747. doi:10.1016/j.jalz.2019.06.2784
- Chen L, Wei Z, Chan KW, et al. Protein aggregation linked to Alzheimer's disease revealed by saturation transfer MRI. *Neuroimage*. 2019;188:380-390.
- Tolomeo D, Micotti E, Serra SC, Chappell M, Snellman A, Forloni G. Chemical exchange saturation transfer MRI shows low cerebral 2-deoxy-D-glucose uptake in a model of Alzheimer's Disease. *Sci Rep*. 2018;8:1-10.
- Wang R, Chen P, Shen Z, et al. Brain amide proton transfer imaging of rat with Alzheimer's disease using saturation with frequency alternating RF irradiation method. *Front Aging Neurosci*. 2019;11:217.
- van Zijl PC, Lam WW, Xu J, Knutsson L, Stanis GJ. Magnetization transfer contrast and chemical exchange saturation transfer MRI. Features and analysis of the field-dependent saturation spectrum. *Neuroimage*. 2018;168:222-241.



31. Henkelman R, Stanisz G, Graham S. Magnetization transfer in MRI: a review. *NMR Biomed*. 2001;14:57-64.
32. Närväinen J, Hubbard PL, Kauppinen RA, Morris GA. Z-spectroscopy with alternating-phase irradiation. *J Magn Reson*. 2010;207:242-250.
33. Zu Z, Janve VA, Xu J, Does MD, Gore JC, Gochberg DF. A new method for detecting exchanging amide protons using chemical exchange rotation transfer. *Magn Reson Med*. 2013;69:637-647.
34. Lee J-S, Regatte RR, Jerschow A. Isolating chemical exchange saturation transfer contrast from magnetization transfer asymmetry under two-frequency RF irradiation. *J Magn Reson*. 2012;215:56-63.
35. Zaiss M, Schmitt B, Bachert P. Quantitative separation of CEST effect from magnetization transfer and spillover effects by Lorentzian-line-fit analysis of z-spectra. *J Magn Reson*. 2011;149:155.
36. Zhou J, Van Zijl PC. Chemical exchange saturation transfer imaging and spectroscopy. *Prog Nucl Magn Reson Spectrosc*. 2006;48:109-136.
37. Jones CK, Polders D, Hua J, et al. In vivo three-dimensional whole-brain pulsed steady-state chemical exchange saturation transfer at 7 T. *Magn Reson Med*. 2012;67:1579-1589.
38. Zhou IY, Wang E, Cheung JS, Zhang X, Fulci G, Sun PZ. Quantitative chemical exchange saturation transfer (CEST) MRI of glioma using Image Downsampling Expedited Adaptive Least-squares (IDEAL) fitting. *Sci Rep*. 2017;7:1-10.
39. Jin T, Wang P, Zong X, Kim SG. MR imaging of the amide-proton transfer effect and the pH-insensitive nuclear Overhauser effect at 9.4 T. *Magn Reson Med*. 2013;69:760-770.
40. Glang F, Deshmene A, Prokudin S, et al. DeepCEST 3T: robust MRI parameter determination and uncertainty quantification with neural networks—application to CEST imaging of the human brain at 3T. *Magn Reson Med*. 2020;84:450-466.
41. Chen L, Schär M, Chan KW, et al. In vivo imaging of phosphocreatine with artificial neural networks. *Nat Commun*. 2020;11:1-10.
42. Li Y, Xie D, Cember A, et al. Accelerating GluCEST imaging using deep learning for B0 correction. *Magn Reson Med*. 2020;84:1724-1733. doi:10.1002/mrm.28289
43. Zaiss M, Deshmene A, Schuppert M, et al. 9.4 T Chemical exchange saturation transfer MRI contrast predicted from 3 T data—a proof of concept study. *Magn Reson Med*. 2019;81:3901-3914.
44. LeCun Y, Bengio Y, Hinton G. Deep learning. *Nature*. 2015;521:436-444.
45. Kim B, Schär M, Park H, Heo H-Y. A deep learning approach for magnetization transfer contrast MR fingerprinting and chemical exchange saturation transfer imaging. *NeuroImage*. 2020;221:117165.
46. Perlman O, Ito H, Herz K, et al. AI boosted molecular MRI for apoptosis detection in oncolytic virotherapy. *bioRxiv*. 2020. doi:10.1101/2020.03.05.977793
47. Guo C, Wu J, Rosenberg JT, Roussel T, Cai S, Cai C. Fast chemical exchange saturation transfer imaging based on PROPELLER acquisition and deep neural network reconstruction. *Magn Reson Med*. 2020;84:3192-3205.
48. Cohen O, Huang S, McMahon MT, Rosen MS, Farrar CT. Rapid and quantitative chemical exchange saturation transfer (CEST) imaging with magnetic resonance fingerprinting (MRF). *Magn Reson Med*. 2018;80:2449-2463.
49. Kang B, Kim B, Schär M, Park H, Heo HY. Unsupervised learning for magnetization transfer contrast MR fingerprinting: application to CEST and nuclear Overhauser enhancement imaging. *Magn Reson Med*. 2021;85:2040-2054.
50. Sui R, Chen L, Li Y, et al. Whole-brain amide CEST imaging at 3T with a steady-state radial MRI acquisition. *Magn Reson Med*. 2021;86:893-906.
51. Rerich E, Zaiss M, Korzowski A, Ladd ME, Bachert P. Relaxation-compensated CEST-MRI at 7T for mapping of creatine content and pH—preliminary application in human muscle tissue in vivo. *NMR Biomed*. 2015;28:1402-1412.
52. Zaiss M, Windschuh J, Goerke S, et al. Downfield-NOE-suppressed amide-CEST-MRI at 7 Tesla provides a unique contrast in human glioblastoma. *Magn Reson Med*. 2017;77:196-208.
53. Zhang XY, Wang F, Li H, et al. Accuracy in the quantification of chemical exchange saturation transfer (CEST) and relayed nuclear Overhauser enhancement (rNOE) saturation transfer effects. *NMR Biomed*. 2017;30:e3716.
54. Tse K-H, Cheng A, Ma F, Herrup K. DNA damage-associated oligodendrocyte degeneration precedes amyloid pathology and contributes to Alzheimer's disease and dementia. *Alzheimers Dement*. 2018;14:664-679.
55. Zaiss M, Bachert P. Chemical exchange saturation transfer (CEST) and MR Z-spectroscopy in vivo: a review of theoretical approaches and methods. *Phys Med Biol*. 2013;58:R221.
56. Möller MF. A scaled conjugate gradient algorithm for fast supervised learning. *Neural Networks*. 1993;6:525-533.
57. Spencer N, Bridges L, Elderfield K, Amir K, Austen B, Howe F. Quantitative evaluation of MRI and histological characteristics of the 5xFAD Alzheimer mouse brain. *Neuroimage*. 2013;76:108-115.
58. Rojas S, Herance JR, Gispert JD, et al. In vivo evaluation of amyloid deposition and brain glucose metabolism of 5XFAD mice using positron emission tomography. *Neurobiol Aging*. 2013;34:1790-1798.
59. Windschuh J, Zaiss M, Meissner JE, et al. Correction of B1-inhomogeneities for relaxation-compensated CEST imaging at 7 T. *NMR Biomed*. 2015;28:529-537.
60. Wang R, Li S-Y, Chen M, et al. Amide proton transfer magnetic resonance imaging of Alzheimer's disease at 3.0 Tesla: a preliminary study. *Chin Med J*. 2015;128:615.
61. Zhang Z, Zhang C, Yao J, et al. Protein-based amide proton transfer-weighted MR imaging of amnesic mild cognitive impairment. *Neuroimage Clin*. 2020;25:102153.
62. Jankowsky JL, Zheng H. Practical considerations for choosing a mouse model of Alzheimer's disease. *Mol Neurodegener*. 2017;12:1-22.
63. Chen L, van Zijl PC, Wei Z, et al. Early detection of Alzheimer's disease using creatine chemical exchange saturation transfer magnetic resonance imaging. *Neuroimage*. 2021;236:118071.
64. Fang B, Wang D, Huang M, Yu G, Li H. Hypothesis on the relationship between the change in intracellular pH and incidence of sporadic Alzheimer's disease or vascular dementia. *Int J Neurosci*. 2010;120:591-595.
65. Schwartz L, Peres S, Jolicœur M, da Veiga MJ. Cancer and Alzheimer's disease: intracellular pH scales the metabolic disorders. *Biogerontology*. 2020;21:683-694.
66. Hanyu H, Asano T, Sakurai H, Takasaki M, Shindo H, Abe K. Magnetization transfer measurements of the hippocampus

- in the early diagnosis of Alzheimer's disease. *J Neurol Sci.* 2001;188:79-84.
67. Kabani NJ, Sled JG, Chertkow H. Magnetization transfer ratio in mild cognitive impairment and dementia of Alzheimer's type. *Neuroimage.* 2002;15:604-610.
  68. Van Es A, Van der Flier W, Admiraal-Behloul F, et al. Magnetization transfer imaging of gray and white matter in mild cognitive impairment and Alzheimer's disease. *Neurobiol Aging.* 2006;27:1757-1762.
  69. Giulietti G, Bozzali M, Figura V, et al. Quantitative magnetization transfer provides information complementary to grey matter atrophy in Alzheimer's disease brains. *Neuroimage.* 2012;59:1114-1122.
  70. Kiefer C, Brockhaus L, Cattapan-Ludewig K, et al. Multi-parametric classification of Alzheimer's disease and mild cognitive impairment: the impact of quantitative magnetization transfer MR imaging. *Neuroimage.* 2009;48:657-667.
  71. Van Der Flier WM, Van Den Heuvel DM, Weverling-Rijnsburger AW, et al. Magnetization transfer imaging in normal aging, mild cognitive impairment, and Alzheimer's disease. *Ann Neurol.* 2002;52:62-67.
  72. Ridha BH, Tozer DJ, Symms MR, et al. Quantitative magnetization transfer imaging in Alzheimer disease. *Radiology.* 2007;244:832-837.
  73. Pérez-Torres CJ, Reynolds JO, Pautler RG. Use of magnetization transfer contrast MRI to detect early molecular pathology in Alzheimer's disease. *Magn Reson Med.* 2014;71:333-338.
  74. Bigot C, Vanhoutte G, Verhoye M, Van der Linden A. Magnetization transfer contrast imaging reveals amyloid pathology in Alzheimer's disease transgenic mice. *Neuroimage.* 2014;87:111-119.
  75. Ohno M, Cole SL, Yasvoina M, et al. BACE1 gene deletion prevents neuron loss and memory deficits in 5XFAD APP/PS1 transgenic mice. *Neurobiol Dis.* 2007;26:134-145.
  76. Cui J, Zu Z. Towards the molecular origin of glutamate CEST (GluCEST) imaging in rat brain. *Magn Reson Med.* 2020;83:1405-1417.

## SUPPORTING INFORMATION

Additional supporting information may be found in the online version of the article at the publisher's website.

**FIGURE S1** Demonstration of slice selections for central and anterior images that were investigated in this study

**FIGURE S2** Determination of regularization parameters  $\gamma$  for (A) deepCEST and (B) deepAREX

**FIGURE S3** Representative CEST/AREX maps of WT and AD brains that were generated by 4PLF/AREX. CEST maps ( $A_{3.5 \text{ ppm}}$ ,  $A_{\text{rNOE}}$ , and  $A_{\text{MT}}$ ) of (A) central and (B) anterior slices. AREX maps ( $R_{3.5 \text{ ppm}}$ ,  $R_{\text{rNOE}}$ , and  $R_{\text{MT}}$ ) of (C) central and (D) anterior slices.  $R_i$  values were presented in  $\text{s}^{-1}$

**FIGURE S4** Group comparing results of CEST/AREX between WT ( $n = 10$ ) and AD ( $n = 10$ ) mice that were generated by 4PLF/AREX. Comparison of CEST parameters ( $A_{3.5 \text{ ppm}}$ ,  $A_{\text{rNOE}}$ , and  $A_{\text{MT}}$ ) between WT and AD for (A) central and (B) anterior slices. Comparison of AREX parameters ( $R_{3.5 \text{ ppm}}$ ,  $R_{\text{rNOE}}$ , and  $R_{\text{MT}}$ ) between WT and AD

for (C) central and (D) anterior slices.  $R_i$  values were presented in  $\text{s}^{-1}$ . Significance levels:  $*P < 0.05$ ,  $**P < 0.01$ , and  $***P < 0.001$

**FIGURE S5** Regression plots of deepCEST/deepAREX with 4PLF/AREX for both CEST parameters ([A] and [B] including  $A_{3.5 \text{ ppm}}$ ,  $A_{\text{rNOE}}$ , and  $A_{\text{MT}}$ ) and AREX parameters ([C] and [D] including  $R_{3.5 \text{ ppm}}$ ,  $R_{\text{rNOE}}$  and  $R_{\text{MT}}$ ) of all WT ([A] and [C]  $n = 10$ ) and AD ([B] and [D]  $n = 10$ ) mouse brains including both central and anterior slices.  $R_i$  values were presented in  $\text{s}^{-1}$ . Outputs were the results of deepCEST/deepAREX, whereas the targets were the results of 4PLF/AREX

**FIGURE S6** The normalized singular value (L-curve) as a function of rank number, generated by multilinear singular value decomposition (MLSVD). Subplot showed the zoom-in vision of singular value curve and linear reference curve

**FIGURE S7** Determination of regularization parameters  $\gamma$  for (A) deepCEST and (B) deepAREX with denoising

**FIGURE S8** Pixel-wise regression plots of denoised CEST parameters ([A]  $\Delta B_0$  in ppm; [B]  $A_{3.5 \text{ ppm}}$ ; [C]  $A_{\text{rNOE}}$ ; [D]  $A_{\text{MT}}$ ) and denoised AREX parameters ([E]  $\Delta B_0$  in ppm; [F]  $R_{3.5 \text{ ppm}}$ ; [G]  $R_{\text{rNOE}}$ ; [H]  $R_{\text{MT}}$ ) for the training data of all WT mice.  $R_i$  values were presented in  $\text{s}^{-1}$ . Outputs were the results of deepCEST/deepAREX with denoising, whereas the targets were the results of 4PLF/AREX with denoising

**FIGURE S9** Pixel-wise regression plots of denoised CEST parameters ([A]  $\Delta B_0$  in ppm; [B]  $A_{3.5 \text{ ppm}}$ ; [C]  $A_{\text{rNOE}}$ ; [D]  $A_{\text{MT}}$ ) and denoised AREX parameters ([E]  $\Delta B_0$  in ppm; [F]  $R_{3.5 \text{ ppm}}$ ; [G]  $R_{\text{rNOE}}$ ; [H]  $R_{\text{MT}}$ ) for the testing data of all AD mice.  $R_i$  values were presented in  $\text{s}^{-1}$ . Outputs were the results of deepCEST/deepAREX with denoising, whereas the targets were the results of 4PLF/AREX with denoising

**FIGURE S10** Results of deepCEST/deepAREX with denoising using CEST data with added Gaussian noise as inputs. Representative Z-spectra interfered by Gaussian noise with different SDs of (A) 0.01 and (B) 0.05. (C) CEST and (D) AREX maps predicted by the deepCEST and deepAREX with denoising, respectively.  $R_i$  values were presented in  $\text{s}^{-1}$ . Only the central slice was used here for demonstration. Numbers inside maps in (C) and (D) indicated the corresponding SNR values of 2 ROIs. SNR values were calculated by:  $\text{SNR} = 20 \times \lg(\text{mean}/\text{SD})$

**FIGURE S11** Consistency checking for deepCEST. (A) The flow of consistency checking. (B) Comparison of Z-spectra 1 and 2, together with (C) comparison of CEST parameters ( $\Delta B_0$  in ppm,  $A_{3.5 \text{ ppm}}$ ,  $A_{\text{rNOE}}$ , and  $A_{\text{MT}}$ ) 1 and 2, generated by the deepCEST network used in Figures 2–7. (D) Comparison of Z-spectra 1 and 2, together with (E) comparison of CEST parameters ( $\Delta B_0$  in ppm,  $A_{3.5 \text{ ppm}}$ ,  $A_{\text{rNOE}}$ , and  $A_{\text{MT}}$ ) 1 and 2, generated by the deepCEST network used in FIGURE 10. Difference (Diff) = Z-spectra 1 – Z-spectra 2

**FIGURE S12** Representative  $B_1$  maps and corresponding  $A_{MT}$  maps of a WT mouse brain, including both central and anterior slices. Red ellipses indicated the regions with slightly low  $A_{MT}$  values that were induced by low  $B_1$  values at the rim

**TABLE S1** Initial values and bound conditions for the 4PLF described in the Methods section

**How to cite this article:** Huang J, Lai JHC, Tse K-H, et al. Deep neural network based CEST and AREX processing: Application in imaging a model of Alzheimer's disease at 3 T. *Magn Reson Med*. 2022;87:1529–1545. doi:[10.1002/mrm.29044](https://doi.org/10.1002/mrm.29044)